Membrane Structure Characterization Using Variable-Period X-Ray Standing Waves

Ruitian Zhang, Rosangela Itri, and Martin Caffrey
Department of Chemistry, The Ohio State University, Columbus, Ohio 43210 USA

ABSTRACT The variable-period x-ray standing wave (XSW) technique is emerging as a powerful tool for studying membrane structure. However, two significant problems arise when the method is used to characterize membranes of thickness $d_L <$ 100 Å. First, the surface roughness, σ_r, of the supporting reflecting mirror convolutes with the intrinsic half-width of the marker atom distribution in the membrane, σ_{in}, and contributes to an apparent half-width, σ, which is measured in the XSW experiment. Here we show how the latter terms are related quantitatively [$\sigma_{in} = (\sigma^2 - \sigma_r^2)^{1/2}$], such that rough mirrors give rise to larger marker atom distribution widths, σ, and how the required quantity σ_{in} can be determined in the XSW measurement. Second, when the mean position of the marker atom layer, $\langle z \rangle$, is close to one or both boundaries of the membrane, its distribution function is truncated at the boundary. In such cases, we show why marker atom distribution should be expressed in terms of its first and second moments. We also demonstrate by numerical simulations of realistic samples how the physical parameters, σ_r, σ, $\langle z \rangle$, and d_L, affect x-ray reflectivity and fluorescence yield profiles as an aid in their interpretation.

INTRODUCTION

The utility of the variable-period x-ray standing wave (XSW) method for characterizing the structure and dynamic properties of membranes has been demonstrated (Bedzyk et al., 1988, 1989, 1990; Wang et al., 1991, 1992, 1994a; Kirchner et al., 1995). X-ray standing waves come about as a result of the interference of an incident x-ray beam and a coherently reflected x-ray beam from a reflecting mirror surface. In the course of a so-called θ-scan, where the angle between the sample and the incident beam, θ, is changed, the XSW nodes and antinodes pass through a mirror-supported adlayer incorporating a marker atom, usually but not always a heavy (high atomic number) atom (Wang and Caffrey, 1995), giving rise to minima and maxima, respectively, in the corresponding x-ray fluorescence yield profile. From this profile, information about the spatial distribution of the marker atom can be obtained.

In early variable-period XSW experiments (Bedzyk et al., 1988, 1989; Wang et al., 1991, 1992), the model membrane films used typically ranged in thickness from several hundred to about a thousand angstroms. The average position, $\langle z \rangle$ (the z direction being normal to the mirror plane), of marker atoms in the marker atom layer above the reflecting mirror were on the same length scale, with an associated spread (half-width at half-height) of 10–20 Å (Wang et al., 1991, 1994a). The technique has also been used to examine more biologically relevant systems, such as phospholipid membranes and membrane-associated proteins (Wang et al., 1994b). Such studies require applying the method to relatively thin adlayers with z dimensions approaching that of the cell membrane, on the order of 50–100 Å. However, in these studies, the interpretation of the experimental data becomes more difficult for two reasons. First, a large mirror surface roughness can lead to a marker atom distribution width within the host membrane large enough to be comparable to $\langle z \rangle$. It is necessary then to deconvolute the intrinsic distribution width of the marker atoms in the film from the measured total distribution. In the current study, we describe the basis for this and how it can be done. The second problem arises as a result of marker atom distributions being truncated by the adlayer boundary. Usually, when the marker atoms are distributed inside a lipid film that is far from the film boundaries, a Gaussian with a mean position, μ_g, and standard deviation, σ_g, is used to describe the marker atom distribution (Bedzyk et al., 1989; Wang et al., 1994a, b; Kirchner et al., 1995). However, when the marker atom layer in the film is close to the film boundaries (which is often the case when the adlayer is as thin as several tens of angstroms), i.e., when $(d_L - \mu_g)/\sigma_g \approx 1$ or $\mu_g/\sigma_g \approx 1$ (d_L is the organic film thickness), the Gaussian is truncated by the boundaries. In this case, quite different values of μ_g and σ_g can yield very similar fluorescence yield profiles (see below). An obvious consequence is that the method becomes less sensitive to marker atom distribution features. The purpose of this paper is to understand and solve these two problems, so that the variable-period XSW technique can be successfully applied to a greater range of thin films, and especially to the more biologically relevant systems where problems of this type are encountered.

The basic theory governing reflection and refraction of x-rays in stratified media, with ideally flat interfaces devoid of interfacial roughness, is well established (Parrat, 1954).

Received for publication 18 August 1997 and in final form 22 December 1997.

Address reprint requests to Dr. Martin Caffrey, Department of Chemistry, The Ohio State University, 120 W. 18th Ave., Columbus, OH 43210. Tel.: 614-292-8437; Fax: 614-292-1532; E-mail: caffrey@chemistry.ohio-state.edu.

Dr. Zhang's present address is Chemistry Division, Argonne National Laboratory, 9700 S. Cass Ave., Argonne, IL 60439.

Dr. Itri's permanent address is Instituto de Fisica da Universidade de São Paulo, C.P. 66318, São Paulo SP 05389-970, Brazil.

0006-3495/98/04/1924/13 $2.00

In the field of x-ray reflectivity, problems associated with surface roughness have been discussed extensively (Nevot and Croce, 1980; Cowley and Ryan, 1987; Sinha et al., 1988; Vidal et al., 1988; Penfold and Thomas, 1990; Dietrich and Haase, 1995). Surface and interfacial roughness effects on x-ray and neutron scattering and on x-ray fluorescence in solid multilayers and layered synthetic microstructures have also been discussed (de Boer, 1991, 1994, 1995, 1996; Krol et al., 1988). In the current application, we extend the discussion of interfacial roughness effects on x-ray scattering/fluorescence to the variable-period XSW technique. Specifically, we show how substrate surface roughness is convoluted into marker atom distribution width, and how the intrinsic distribution width can be extracted from the measured width.

Our report is organized as follows. First, the basic theory of x-ray scattering/reflectivity at flat and at rough interfaces is reviewed in brief. The problems introduced by interfacial roughness are then discussed. After this, numerical simulations are used to show how marker atom distribution features (mean position, distribution width), total adlayer thickness, and mirror roughness affect the x-ray reflectivity and fluorescence profiles.

THEORY

The theory of x-ray scattering at flat interfaces is well established. Elements of this theory as it applies to the XSW method are summarized below. Additional details can be found in the appropriate references (Parrat, 1954; Wang, 1994).

Refractive indices of electromagnetic media in the x-ray regime

When x-rays travel from one electromagnetic medium to another with a different refractive index, scattering takes place at the interface. The refractive index of an electromagnetic medium for x-rays can be written as

$$n = 1 - \delta - i\beta, \tag{1}$$

where δ is the refractive index decrement and β is the absorption index. Both δ and β are small quantities (δ is on the order of 10^{-5} or smaller, and typically $\beta/\delta \leq 0.1$ for hard x-rays). δ and β are calculated as follows: $\delta = (f_0 + \Delta f')N_A r_e \lambda^2/2\pi$ and $\beta = (\Delta f'')N_A r_e \lambda^2/2\pi = \mu\lambda/(4\pi)$, where N_A (Å^{-3}) is atom number density; r_e (= 2.8×10^{-5} Å) is the classical Thompson radius of the electron; λ (Å) is the x-ray wavelength; f_0, $\Delta f'$, $\Delta f''$ are the normal, resonance, and absorption scattering factors, respectively; and μ (cm^{-1}) is the linear absorption coefficient of the material for x-rays. The critical angle, θ_c, of an x-ray reflecting mirror is customarily defined such that for x-rays striking the mirror from air at θ_c, the angle of refraction is zero. For x-rays entering medium 2 ($n_2 = 1 - \delta - i\beta$, $\theta_2 = 0$) from air ($n_1 = 1$, $\theta_1 = \theta_c$), Snell's law ($n_1 \cos\theta_1 = n_2 \cos\theta_2$) yields the following relation, when the minuscule β term is neglected:

$$\cos\theta_c = 1 - \delta, \tag{2}$$

such that

$$\theta_c = \cos^{-1}(1 - \delta) \approx (2\delta)^{1/2}, \quad (\delta \ll 1). \tag{3}$$

θ_c is a very important quantity as far as variable-period XSWs are concerned, in that it characterizes the x-ray optical property of a material, as will be shown below.

X-ray electric field and fluorescence intensity for systems with flat interfaces

The angle of refraction of an x-ray beam striking a surface or interface in a multilayer system at a grazing incident angle, θ_1, in an arbitrary mth layer, can be calculated by using Snell's law as (Parrat, 1954; Wang, 1994)

$$\theta_m = (\theta_1^2 - 2\delta_m - 2i\beta_m)^{1/2}, \quad (m = 1, \ldots, N) \tag{4}$$

where N is the total number of layers, and m is the index of the layer. Equation 4 is used in deriving formulas below (Eqs. 5–19), which are used to calculate x-ray reflectivity and electric field intensity.

Two-layer system with a single flat interface

The simplest system of this type consists of a single flat interface separating two media, as in Fig. 1. The amplitudes of the incident, reflected, and transmitted electric fields are E_1, E_1^R, and E_2, respectively. Because θ_1 is the angle that is actually adjusted in the XSW experiment, and is used throughout our theoretical discussions, we will refer to it hereafter simply as θ. Note that $\delta_1 = \beta_1 = 0$ for a vacuum and that $\delta_1 \approx 0$ and $\beta_1 \approx 0$ for air. Using the continuity of the electric and magnetic fields at the interface, and the

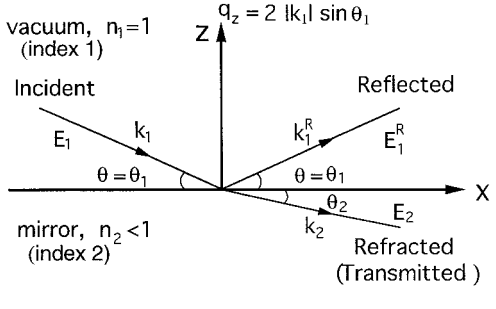

FIGURE 1 Reflection and refraction (transmission) of x-rays at an interface between vacuum (air) and a mirror. k_1 and k_1^R are, respectively, the incident and reflected wave vectors of the x-rays in vacuum (air), and k_2 is the refracted wave vector in the mirror. $\theta_1 \equiv \theta$ is the incident angle, and θ_2 is the angle of refraction. E_1, E_1^R, and E_2 are the electric fields of the incident, reflected, and refracted (transmitted) x-rays, respectively, all of which are perpendicular to the incident (x-z) plane. The refractive index, n, of the two media is also indicated in the figure. q_z is the z component of the momentum transfer in vacuum (air).

definition in Eq. 4, the reflection coefficient is given by (Parrat, 1954)

$$r(\theta) = \frac{E_1^R}{E_1} \approx \frac{\theta - \theta_2}{\theta + \theta_2} = \frac{\theta - (\theta^2 - 2\delta_2 - 2i\beta_2)^{1/2}}{\theta + (\theta^2 - 2\delta_2 - 2i\beta_2)^{1/2}}, \quad (5)$$

where θ_2 is the refractive angle in medium 2. The reflectivity is

$$R(\theta) = |r(\theta)|^2. \quad (6)$$

The amplitude of an x-ray standing wave electric field at position z above a mirror surface is given by the superposition of the incident and reflected x-ray electric field: $E = E_1^R + E_1$. The corresponding intensity is (Bedzyk et al., 1989)

$$I(\theta, z) = |E_1^R + E_1|^2 = I_0[1 + R(\theta) + 2(R(\theta))^{1/2}\cos(\Phi(\theta) - 2\pi z/D(\theta))], \quad (7)$$

where I_0 is the intensity of the incident x-ray beam; $\Phi(\theta)$ (= $\tan^{-1}[\mathrm{Im}(r(\theta))/\mathrm{Re}(r(\theta))]$) is the phase shift between the reflected and incident rays; $\mathrm{Im}(r(\theta))$ and $\mathrm{Re}(r(\theta))$ are the imaginary and real part of $r(\theta)$, respectively; and $D(\theta)$ (= $\lambda/(2\sin\theta)$) is the period of the standing wave field corresponding to the distance between two adjacent nodes (or antinodes) in the XSW electric field. Consequently, the period at θ_c is the critical period, D_c (= $\lambda/(2\sin\theta_c)$). $D(\theta)$ can be viewed as the unit length of the standing wave field "yardstick" used to measure marker atom layer position. For the gold mirrors used in typical XSW experiments (θ_c = 7.73 mrad) and x-rays with an energy of 9.8 keV (λ = 1.265 Å) (Itri et al., 1997), $D_c \approx 82$ Å. Note that in this single interface case, the standing wave electric field intensity, $I(\theta, z)$, and the measured reflectivity, $R(\theta)$, are directly related, as indicated in Eq. 7. The relationship between electric field intensity and the measured reflectivity for multilayer systems is more complex, as shown below. Once the electric field intensity in Eq. 7 has been determined, the x-ray fluorescence yield from the marker atoms can be obtained by using the following integration:

$$\Upsilon(\theta) = \int \rho(z) I(\theta, z) dz. \quad (8)$$

where $\rho(z)$ is the distribution function of the marker atoms in the organic adlayer in the z direction.

Multilayer system with flat interfaces

In real samples of the type studied in this group by means of the variable-period XSW technique, marker atoms are usually incorporated into lipid and/or protein molecules. This means that, in practice, we deal with multilayer systems (consisting of air, organic adlayer, reflecting mirror, and other support materials) in XSW experiments. When there are multiple flat interfaces in the system, the electric field intensities are best calculated by using the recursion formula (Parrat, 1954). Consequently, the mathematics are more complicated, and an understanding of the effects of various physical parameters on x-ray reflectivity and fluorescence yield relies heavily on numerical calculations, as detailed below. Here we review the relevant analytical formulas.

For any three adjacent layers in an N-layer system (see Fig. 2), the Fresnel reflection coefficient, $F^R_{m-1,m}$, and transmission coefficient, $F^T_{m-1,m}$, are defined, respectively, as

$$F^R_{m-1,m} = \frac{\theta_{m-1} - \theta_m}{\theta_{m-1} + \theta_m}, \quad (9)$$

and

$$F^T_{m-1,m} = \frac{2\theta_{m-1}}{\theta_{m-1} + \theta_m}, \quad (m = 1, \ldots, N), \quad (10)$$

where θ_{m-1} and θ_m are calculated using Eq. 4. Defining the effective reflection coefficient at interface (m, $m + 1$) as $r_{m,m+1} = E^R_m/E_m$, it has been shown that the following recursion formula holds for the coefficients $r_{m-1,m}$ and $r_{m,m+1}$ (Parrat, 1954):

$$r_{m-1,m} = \frac{F^R_{m-1,m} + r_{m,m+1}\exp(-2ik_1\theta_m d_m)}{1 + F^R_{m-1,m}[r_{m,m+1}\exp(-2ik_1\theta_m d_m)]}, \quad (11)$$

where k_1 (= $2\pi/\lambda$) is the wave vector in air, and d_m is the thickness of layer m measured in the z direction. Starting from the bottom layer with $r_{N,N+1}$, and repeatedly using Eq. 11, the measured reflectivity at the air/multilayer interface is

$$R_{1,2}(\theta) = |r_{1,2}(\theta)|^2. \quad (12)$$

Next, the electric field intensity, $I_m(\theta, z)$, at position z above interface (m, $m + 1$) is calculated as the superposition

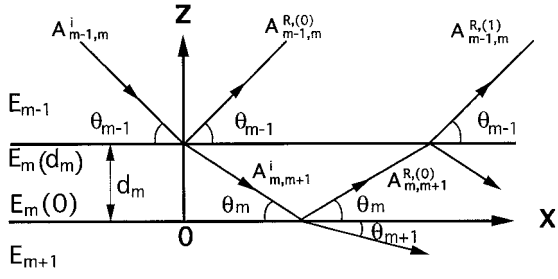

FIGURE 2 Ray trace diagram of x-rays for three adjacent layers ($m - 1$, m, and $m + 1$) in a multilayer system. $A^i_{m-1,m}$ represents the complex amplitude of the incident x-rays striking interface ($m - 1$, m) from layer ($m - 1$); $A^{R,(0)}_{m-1,m}$ represents the complex amplitude of x-rays reflected directly from interface ($m - 1$, m) back into layer ($m - 1$) without penetrating layer m; $A^{R,(1)}_{m-1,m}$ represents the complex amplitude of x-rays transmitted back into layer ($m - 1$) from interface ($m - 1$, m) after traveling once into and then back out of layer m. $A^i_{m,m+1}$ and $A^{R,(0)}_{m,m+1}$ refer to layers m and $m + 1$ in the same way that $A^i_{m-1,m}$ and $A^{R,(0)}_{m-1,m}$ refer to layers ($m - 1$) and m. The origin of the z coordinate is at the interface (m, $m + 1$). The thickness of layer m is d_m. The amplitude of the electric field in layer m is $E_m(0)$ just above the (m, $m + 1$) interface and $E_m(d_m)$ just below the ($m - 1$, m) interface. The electric fields in layers ($m - 1$) and ($m + 1$) are E_{m-1} and E_{m+1}, respectively.

of the electric field of the incident and reflected x-rays in layer m (Wang, 1994):

$$I_m(\theta, z) = |E_m(d_m)|^2 \exp(-2k_1 B_m d_m)[\exp(2k_1 B_m z) + R_{m,m+1}\exp(-2k_1 B_m z) + 2(R_{m,m+1})^{1/2}\cos(\Phi_m^R - 2k_1 A_m z)], \quad (13)$$

where Φ_m^R ($= \tan^{-1}[\mathrm{Im}(r_{m,m+1})/\mathrm{Re}(r_{m,m+1})]$) is the phase shift between the reflected and incident rays; $A_m = \mathrm{Re}(\theta_m)$, $B_m = -\mathrm{Im}(\theta_m)$, and

$$R_{m,m+1} = |r_{m,m+1}|^2, \quad (14)$$

is the reflectivity at the $(m, m + 1)$ interface. $E_m(d_m)$ is the amplitude of the electric field below interface $(m - 1, m)$ and at a distance d_m above interface $(m, m + 1)$ in layer m. Before describing how $E_m(d_m)$ is calculated, it is useful to define the effective transmission coefficient as

$$t_{m-1,m} = E_m(d_m)/E_{m-1}(d_{m-1}). \quad (15)$$

Then, $t_{m-1,m}$ can be calculated as (Wang, 1994)

$$t_{m-1,m} = (1 - F^R_{m-1,m} r_{m-1,m})[\exp(ik_1\theta_{m-1}d_{m-1})]/F^T_{m-1,m}. \quad (16)$$

Starting from the very top air/multilayer interface with $E_{m=1} = E_1$, the electric field $E_m(d_m)$ can be calculated as

$$E_m(d_m) = E_1 \prod_{j=2}^{m} t_{j-1,j}. \quad (17)$$

Equations 13–17 can be used to calculate the electric field intensity at an arbitrary position in a multilayer system.

For typical samples used in XSW experiments, marker atoms are incorporated into organic thin films on solid substrates, which constitute, respectively, the second ($m = 2$) and third ($m = 3$) layers in a multilayer system. (We note that the marker atom layer can be neglected as a layer in these applications because it has an insignificant effect on the standing-wave electric field (Wang, 1994). Therefore, it is worthwhile to present the formulas used to calculate the electric field intensities in such a system.) Because the absorption index of a lipid is much smaller than its refractive index decrement, i.e., $\beta_2/\delta_2 < 0.001$ (Wang et al., 1992), to a very good approximation, we can set $\beta_2 = 0$. Then, from Eqs. 3 and 4 and 13–17, for $\theta > \theta_{2c}$, $A_2 = (\theta^2 - \theta_{2c}^2)^{1/2}$, $B_2 = 0$, and the electric field intensity inside the organic adlayer is

$$I_2(\theta, z) = |E_2(d_2)|^2[1 + R_{2,3}(\theta) + 2(R_{2,3}(\theta))^{1/2}\cos(\Phi_2^R(\theta) - 2k_1 z(\theta^2 - \theta_{2c}^2)^{1/2})], \quad (\theta > \theta_{2c}), \quad (18)$$

where $R_{2,3}(\theta)$ is the reflectivity at the lipid/mirror interface (Eq. 14), and d_2 ($\equiv d_L$) is the thickness of the organic adlayer. Correspondingly, for $\theta \le \theta_{2c}$, $B_2 = (\theta_{2c}^2 - \theta^2)^{1/2}$ and $A_2 = 0$. Therefore,

$$I_2(\theta, z) = |E_2(d_2)|^2 \exp(-2k_1 d_2(\theta_{2c}^2 - \theta^2)^{1/2}) \cdot [1/W + R_{2,3}(\theta)W - 2(R_{2,3}(\theta))^{1/2}], \quad (\theta \le \theta_{2c}), \quad (19)$$

where $W = \exp(-2k_1 z(\theta_{2c}^2 - \theta^2)^{1/2})$. Note that in this angular range ($\theta \le \theta_{2c}$), the electric field intensity $I_2(\theta, z)$ changes exponentially with z, and not as a cosine function as in Eq. 18. Therefore, instead of a standing-wave field, an evanescent wave field is formed inside the organic adlayer below its critical angle. Physically, this arises because of the fact that "total" external reflection occurs at the air/adlayer interface, and x-rays incident at $\theta \le \theta_{2c}$ can penetrate the adlayer with an exponentially decreasing intensity, thereby forming the evanescent wave field.

It is evident that the electric field intensity $I_2(\theta, z)$ in Eqs. 18 and 19 and the measured reflectivity, $R_{1,2}(\theta)$, are not directly related, as they are in Eq. 7 for a single interface. Rather, they are indirectly related through the intermediate quantity $R_{2,3}(\theta)$ (Eq. 14). To show quantitatively how the lipid adlayer changes the relationship between the x-ray reflectivity and XSW electric field intensity, a calculation of the angular dependence of reflectivity, $R(\theta)$, and of the electric field intensity, $I(\theta, z)$, measured at $z = 50$ Å above a bare flat gold mirror surface in air is presented in Fig. 3. For comparison, we also show the corresponding calculation of the reflectivity, $R_{1,2}(\theta)$, and intensity, $I_2(\theta, z = 50$ Å), for the same gold mirror upon which is deposited a 100-Å-thick Langmuir-Blodgett film. The two reflectivity curves are very similar and differ by less than 5% over the

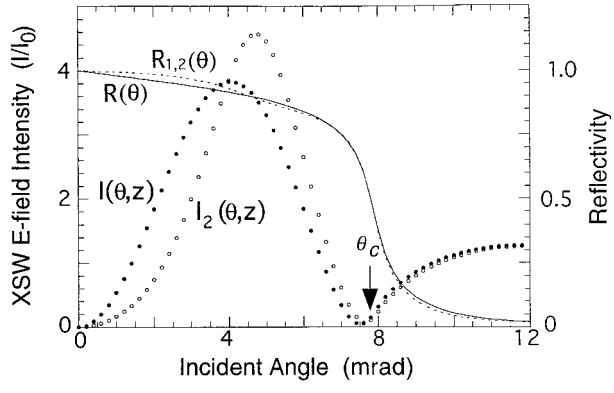

FIGURE 3 The effect of an organic adlayer on a mirror surface on x-ray reflectivity and standing-wave electric field intensity. Reflectivity, $R(\theta)$ (*solid line*), and standing-wave electric field intensity, $I(\theta, z)$ (*solid circles*) at $z = 50$ Å above the gold mirror surface, were calculated using Eqs. 5–7 for a flat, two-layer (air/gold on bulk silicon) system. Similar reflectivity, $R_{1,2}(\theta)$ (*dashed line*), and intensity, $I_2(\theta, z)$ (*open circles*) at $z = 50$ Å calculations using Eqs. 11–12 and 18–19 were performed for a three-layer system consisting of air/lipid/gold on bulk silicon. The values used in the calculations: organic adlayer thickness, $d_L = 100$ Å; gold mirror thickness, $d_{gold} = 1000$ Å; refractive indices for gold, $\delta = 2.99 \times 10^{-5}$, $\beta = 2.20 \times 10^{-6}$; for the organic adlayer, $\delta = 2.50 \times 10^{-6}$, $\beta = 2.24 \times 10^{-9}$; and for bulk silicon, $\delta = 3.80 \times 10^{-6}$, $\beta = 4.00 \times 10^{-7}$ (Itri et al., 1997). The critical angle of the gold mirror is $\theta_c = 7.73$ mrad (indicated by the *arrow*), and that of the lipid adlayer is $\theta_{2c} = 2.24$ mrad. The x-ray wavelength is $\lambda = 1.265$ Å.

entire angular range studied. In contrast, the two electric field intensity curves for $I_2(\theta, z)$ and $I(\theta, z)$ are quite distinct. Besides other, more subtle differences, the $I_2(\theta, z)$ curve is shifted considerably in θ compared to the $I(\theta, z)$ curve. This effect is mainly due to the refraction of x-rays inside the organic adlayer. Later, we show how this effect can be used experimentally to determine d_2 (also referred to as d_L in this work).

The fluorescence yield profile, $\Upsilon(\theta)$, associated with the marker atoms distributed in layer m of a multilayer system with flat interfaces, is calculated from Eq. 13 as

$$\Upsilon(\theta) = \int \rho(z) I_m(\theta, z) dz. \quad (20)$$

X-ray reflectivity at rough interfaces

Surface and interfacial roughness effects on x-ray scattering have been treated extensively in studies of x-ray reflectivity (Nevot and Croce, 1980; Sinha et al., 1988; Vidal et al., 1988; Krol et al., 1988; de Boer, 1991, 1994) and grazing-incidence x-ray fluorescence (de Boer, 1996). In the latter, a highly collimated and monochromatic x-ray beam strikes a sample consisting of a layered solid at grazing incident angles. The fluorescent x-rays from each layer within the solid are detected as a function of incident angle. By comparison, samples used in a variable-period XSW experiment are mostly of the soft condensed matter type, incorporating relatively small amounts (mono- or submonolayer) of fluorescence marker atoms that have little perturbing effect on the electric field. In contrast, interfacial roughness has a pronounced effect on the variable-period XSW method. The latter has not been treated extensively before. We focus on it here by way of better understanding how interfacial roughness affects x-ray reflectivity and fluorescence.

A rough interface can be modeled as a Gaussian distribution of the heights of small flat facets that make up the interface (Sinha et al., 1988; de Boer, 1994; Kirchner et al., 1995) (see Fig. 4 *A* for definitions) as follows:

$$P(z') = \frac{1}{(2\pi)^{1/2}\sigma_r} \exp(-z'^2/2\sigma_r^2), \quad (21)$$

where σ_r is the root mean square interfacial roughness, and z' is the height deviation of an arbitrary facet from the average position of all facets along the interface at $z' = 0$. The most common approach for calculating the x-ray reflectivity for systems with rough interfaces uses the formulas for x-ray optics at flat interfaces as a starting point and treats interfacial roughness as small perturbations on flat interfaces (de Boer, 1996). Two types of roughness factor have been discussed in the literature (de Boer, 1994): the Debye-Waller and the Nevot-Croce factors. The latter takes into account refraction in the mirror, whereas the former does not.

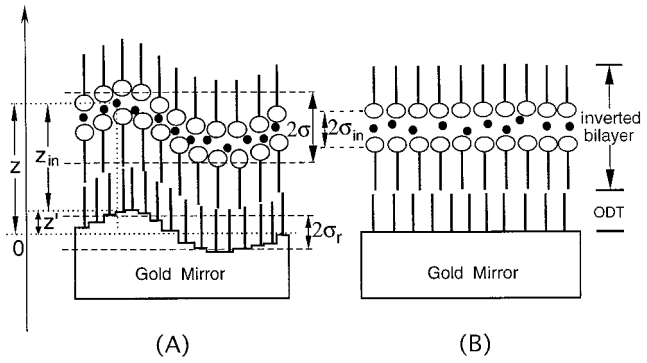

FIGURE 4 Schematic representation of a typical lipid sample used in x-ray standing-wave measurements and how interfacial roughness, σ_r, convolutes with intrinsic marker atom spread, σ_{in}, in the marker atom distribution that is actually measured, σ. Mirror roughness is illustrated in *A* as a series of vertically displaced facets whose surfaces lie parallel to the *x-y* plane. The *z* direction is normal to this surface. The average mirror surface height is assigned a *z* value of zero. z' refers to the distance from this average height to the height of a given facet at the mirror surface. z_{in} is the vertical distance separating a marker atom from the surface of a facet in the mirror directly below it. Marker atoms, lipid molecules, and octadecanethiol (ODT) are represented by solid circles, lollipop figures, and vertical lines, respectively. *A* and *B* represent the sample before and after mirror roughness has been deconvoluted.

The Debye-Waller factor

The original treatment of interfacial roughness made use of what is referred to as the Debye-Waller factor, r_{DW}, defined as (de Boer, 1991)

$$r_{DW} = \exp(-q_z^2\sigma_r^2/2), \quad (22)$$

where $q_z = 4\pi\sin\theta/\lambda$ is the wave vector transfer of the x-ray beam at the air/film interface (see Fig. 1). In the electric field calculation across a series of interfaces, the Fresnel reflection coefficient (Eq. 9) is multiplied by r_{DW} as follows:

$$F^R_{m-1,m}(\sigma_r) = r_{DW} \cdot F^R_{m-1,m}(\sigma_r = 0), \quad (23)$$

where $F^R_{m-1,m}$ $(\sigma_r = 0)$ and $F^R_{m-1,m}(\sigma_r)$ are the Fresnel reflection coefficients at the $(m - 1, m)$ flat and rough interfaces, respectively. For most of the variable-period XSW data analysis reported previously, r_{DW} has been used because of its simplicity.

The Nevot-Croce factor, r_{NC}

For surfaces with small roughness ($q_z\sigma_r/2 < 1$) (for rougher interfaces see de Boer, 1996), or when the incident angle θ is much larger than θ_c, Nevot and Croce (1980) derived a roughness factor of the form

$$r_{NC} = \exp(-q_z q_z^t \sigma_r^2/2), \quad (24)$$

where $q_z^t = 4\pi\sin\theta_t/\lambda$ is the wave vector transfer of the transmitted rays and θ_t is the angle of the transmitted rays. For grazing incident angles ($\theta \ll 1°$), $q_z^t \approx 4\pi\theta_t/\lambda = 4\pi(\theta^2 - \theta_c^2 - 2i\beta)^{1/2}/\lambda$, from Eq. 4. For x-ray scattering at

interfaces in a multilayer system, Eq. 24 becomes (Cowley and Ryan, 1987; Krol et al., 1988; de Boer, 1996)

$$r_{NC} = \exp(-q_{z,m}q_{z,m+1}\sigma_{r,m}^2/2), \quad (25)$$

where $q_{z,m} \approx 4\pi\theta_m/\lambda$, $q_{z,m+1} \approx 4\pi\theta_{m+1}/\lambda$, and θ_m and θ_{m+1} are the incident angles of the x-rays in layers m and $m + 1$, respectively (Fig. 2), and $\sigma_{r,m}$ is the roughness parameter of the (m, $m + 1$) interface. In practice, $\sigma_{r,m}$ is likely different for different interfaces. However, for simplicity, we assume that $\sigma_{r,m}$ and σ_r are equivalent for the multilayer systems under investigation. As applies in the case with r_{DW} in Eq. 23, the r_{NC} factor is multiplied by the Fresnel reflection coefficient (Eq. 9) to account for interfacial roughness of the Nevot-Croce type.

de Boer (1996) has compared the effects of r_{NC} (Eq. 25) and r_{DW} (Eq. 22) on reflectivity for identical values of σ_r. The results show that r_{DW} attenuates reflectivity more than r_{NC}. For purposes of analyzing current XSW data, it is necessary to determine which of these two models is more appropriate. To this end, we compared fits obtained using r_{DW} and r_{NC} for a set of typical reflectivity data in Fig. 5. The best fitting parameters are presented in Table 1. Fig. 5 shows that the Nevot-Croce model fits the reflectivity profile better. Furthermore, the parameters from the fit (Table 1) using r_{NC} are physically more reasonable. For example, the organic adlayer thickness, d_L, obtained by using r_{NC}, is 75 ± 5 Å, which is close to the calculated maximum thickness (80 Å, hydrocarbon chains in the LB film are assumed to be fully extended in the all-*trans* configuration and oriented with their long axis perpendicular to the mirror surface; Itri et al., 1997). The corresponding d_L value obtained by using the Debye-Waller factor is 101 Å, which is clearly unphysical. The roughness parameter, σ_r, obtained by using r_{NC}, is 12.7 Å, as opposed to 4.5 Å, obtained by using r_{DW}. For comparison, the experimentally measured surface roughness for a thin gold layer ($d \geq 350$ Å) deposited on an aluminum substrate is in the range of 10–15 Å, as determined by scanning tunneling microscopy (Garnaes et al., 1990). These results indicate that the surface roughness parameter obtained by using r_{NC} as opposed to r_{DW} is more reasonable. We conclude, therefore, that the Nevot-Croce factor, r_{NC}, is preferred to the Debye-Waller factor, r_{DW}, for treating roughness of multilayer systems on solid substrates of the type used in the current variable-period XSW studies.

TABLE 1 Best fitting parameters for reflectivity data, using the Nevot-Croce and the Debye-Waller factors to correct interfacial roughness

Model	Parameter			
	$\Delta\theta$ (mrad)*	σ_r (Å)#	d_L (Å)§	χ_v^2¶
Nevot-Croce	−0.23 ± 0.01	12.7 ± 0.3	75 ± 5	1.8
Debye-Waller	−0.15 ± 0.02	4.5 ± 0.1	101 ± 5	5.4

Sample composition and experimental details are in the legend to Fig. 5. The angular fitting range was 3–9 mrad.

*$\Delta\theta$ is referred to as the angular shift. It corresponds to the mismatch in the incident angle between the theoretical model and the experimental data for both x-ray reflectivity and fluorescence yield profile data (Itri et al., 1997).

#σ_r, Interfacial roughness of the multilayer system.

§d_L, Thickness of the organic adlayer.

¶χ_v^2, Reduced χ^2, where v is the number of data points minus the number of fitting parameters.

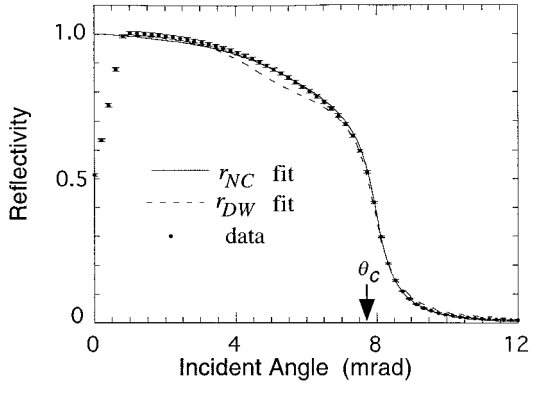

FIGURE 5 Experimental (*circles*) and theoretical (*lines*) x-ray reflectivity profiles for a multilayer sample in air consisting of an inverted bilayer of zinc arachidate on an octadecanethiol monolayer self-assembled on a 1000-Å-thick gold mirror (Itri et al., 1997). The data were fit in the 3–9-mrad angular range using the Nevot-Croce, r_{NC} (*solid line*), and Debye-Waller, r_{DW} (*dashed line*), factors to account for mirror surface roughness, using Eqs. 25 and 22, respectively. The critical angle of the gold mirror, θ_c, is indicated. The following conditions for the experimental and theoretical aspects of the work apply: x-ray wavelength, 1.265 Å; refractive indices for gold, lipid, and silicon are as reported in the legend to Fig. 3. Data were collected at beam line X15A of the National Synchrotron Light Source (NSLS) of Brookhaven National Laboratory, using a highly collimated and monochromatic x-ray beam and a pin diode detector. See Itri et al. (1997) for complete details.

Certainly, r_{NC} represents an approximation for treating the roughness effect. As such, it has its own limitations. In what follows, we evaluate the range of θ in which r_{NC} in Eq. 25 is valid. Because r_{NC} is generally a complex function, we consider its magnitude $|r_{NC}|$ and apply the model to a system consisting of a lipid/gold interface. The layer indices are $m = 3$ for gold, $m = 2$ for lipid, and $m = 1$ for air, and the critical angles are $\theta_{3c} = 7.73$ mrad and $\theta_{2c} = 2.24$ mrad, respectively. It is convenient to consider the roughness effect as applied to the following three angular ranges: $\theta < \theta_{2c}$, $\theta_{2c} < \theta < \theta_{3c}$, and $\theta > \theta_{3c}$. First of all, r_{NC} has been shown to work well in the range $\theta > \theta_{3c}$ (Cowley and Ryan, 1987; de Boer, 1996; and Fig. 5). Then, for $\theta_{2c} < \theta < \theta_{3c}$, we obtain $q_{z,2} \approx 4\pi/\lambda[(\theta^2 - \theta_{2c}^2)^{1/2} - i\beta_2/(\theta^2 - \theta_{2c}^2)^{1/2}]$ and $q_{z,3} \approx 4\pi/\lambda\ [\beta_3/(\theta_{3c}^2 - \theta^2)^{1/2} - i(\theta_{3c}^2 - \theta^2)^{1/2}]$ from the definitions in Eqs. 4 and 25. Because $\beta_2 \ll \theta_{2c}$, $\beta_3 \ll \theta_{3c}$, and $\beta_2 \ll \beta_3$, we obtain $|r_{NC}| \approx \exp[-2(2\pi\sigma_r/\lambda)^2\ \beta_3(\theta^2 - \theta_{2c}^2)^{1/2}/(\theta_{3c}^2 - \theta^2)^{1/2}] < 1$. Therefore, in this angular range, the r_{NC} factor is physically meaningful and serves to reduce the reflectivity to a degree that increases with σ_r. Finally, for $\theta < \theta_{2c}$, where the evanescent wave field is formed in the lipid adlayer, we have $q_{z,2} \approx 4\pi/\lambda[\beta_2/(\theta_{2c}^2 - \theta^2)^{1/2} - i(\theta_{2c}^2 - \theta^2)^{1/2}]$, $q_{z,3} \approx 4\pi/\lambda[\beta_3/(\theta_{3c}^2 - \theta^2)^{1/2} - i(\theta_{3c}^2 - \theta^2)^{1/2}]$, and $|r_{NC}| \approx \exp[2(2\pi\sigma_r/\lambda)^2\ (\theta_{2c}^2 - \theta^2)^{1/2}\ (\theta_{3c}^2 - \theta^2)^{1/2}] > 1$. The latter indicates that reflectivity increases

with roughness! Therefore, r_{NC} is not physically meaningful and should not be used in this angular range. Moreover, this artifact in r_{NC} translates into others, such as the sharp inflection seen at $\theta_{2c} = 2.24$ mrad in some of the calculated fluorescence yield profiles (for instance, in Fig. 11).

The effect of interface roughness on marker atom distribution

A schematic drawing of a marker atom-containing membrane on a solid substrate is shown in Fig. 4 *A*. In practice, such adlayers are deposited on mirrors with finite characteristic roughness. As noted, roughness reduces the intensity of reflected x-rays, and the effect is typically accounted for by a roughness-related factor. The distribution function of marker atoms within the marker atom layer (with a characteristic width, which is referred to as an apparent width, 2σ) corresponds to a local distribution function (with what is referred to as an intrinsic width, $2\sigma_{in}$) horizontally averaged over the whole interface (see Fig. 4 *A*). What we are really interested in is σ_{in}. It is obtained by deconvoluting the measured σ, as described below.

Let us consider the sample shown schematically in Fig. 4 *A*, which illustrates the idea of roughness we wish to convey and the coordinate system we are dealing with. The position of a marker atom with respect to the average height of the mirror surface is z, the height of the mirror surface directly below this marker atom is z', and the height of the marker atom with respect to z' is z_{in}. The origin of the coordinate system is defined such that the average height of the mirror surface is zero, i.e., $\langle z' \rangle = 0$. Therefore, by definition,

$$z = z' + z_{in}. \tag{26}$$

We assume that both z' and z_{in} are distributed randomly. Then, for an ensemble average, Eq. 26 becomes

$$\langle z \rangle = \langle z' \rangle + \langle z_{in} \rangle = \langle z_{in} \rangle, \tag{27}$$

because, by definition, $\langle z' \rangle = 0$. Equation 27 shows that the mean apparent position, $\langle z \rangle$, and the mean intrinsic position, $\langle z_{in} \rangle$, are the same, as expected. Furthermore, for simplicity we assume that z' and z_{in} are distributed independently, such that $\langle z_{in} z' \rangle = \langle z_{in} \rangle \langle z' \rangle = 0$. (A situation where this assumption does not hold is considered below.) Then, averaging the squares of both sides of Eq. 26, we obtain

$$\langle z^2 \rangle = \langle z'^2 \rangle + \langle z_{in}^2 \rangle + 2\langle z_{in} \rangle \langle z' \rangle = \langle z'^2 \rangle + \langle z_{in}^2 \rangle. \tag{28}$$

Subtracting the square of Eq. 27 from Eq. 28, we obtain

$$[\langle z^2 \rangle - \langle z \rangle^2] = [\langle z_{in}^2 \rangle - \langle z_{in} \rangle^2] + \langle z'^2 \rangle. \tag{29}$$

The variance in z is defined as $\sigma^2 = \langle z^2 \rangle - \langle z \rangle^2$ for the apparent distribution and $\sigma_{in}^2 = \langle z_{in}^2 \rangle - \langle z_{in} \rangle^2$ for the intrinsic distribution. From the definition of surface roughness in Eq. 21, $\sigma_r^2 = \langle z'^2 \rangle$. Then, Eq. 29 reduces to

$$\sigma^2 = \sigma_{in}^2 + \sigma_r^2. \tag{30}$$

Equation 30 shows that the roughness of the mirror surface, σ_r, is convoluted into the apparent half-width, σ, from which the desired quantity σ_{in} must be obtained. Fig. 4 *B* illustrates the situation after the interfacial roughness has been deconvoluted from the multilayer sample in Fig. 4 *A*.

An obvious consequence of Eq. 30 is that the intrinsic half-width, σ_{in}, is less than the apparent half-width, σ, obtained by fitting the experimental fluorescence yield profile. By way of example, for a sample with a single bilayer of fatty acid salt on a monolayer of octadecanethiol (ODT) and 1000 Å of gold used in earlier work (Itri et al., 1997), reflectivity data analysis gave $\sigma_r = 12.9$ Å, and the fluorescence yield data fit gave $\sigma = 16.3$ Å. Substituting these two values into Eq. 30 gives an intrinsic half-width, σ_{in}, of 10.0 Å, which is obviously less than σ. In a more recent version of the same measurement (unpublished data), for which mirrors with 280 Å of gold were used, values of $\sigma_r = 5.6$ Å were obtained from the reflectivity data, $\sigma \approx 7$ Å from the fluorescence yield data, and a value of $\sigma_{in} = 4.2$ Å from Eq. 30. Comparing these results from the two experiments, we note that mirrors with larger interfacial roughness, σ_r, had a larger intrinsic distribution half-width, σ_{in}. This suggests that interfacial roughness not only increases σ directly from the convolution in Eq. 30, it also results in a larger σ_{in}. Physically, if the mirror surface is rough, it is unlikely that the lipid molecules deposited on the mirror will follow exactly the roughness profile of the surface (as illustrated in Fig. 4 *A*). Accordingly, surface roughness may induce some degree of packing disorder, which in turn gives rise to increased disorder in the intrinsic distribution of the marker atoms associated with the lipid molecules. This is pure speculation based on a very limited set of data. Nonetheless, it does make sense that σ_{in} can be minimized by using mirrors with the lowest σ_r.

It is well known that for gold mirrors prepared by thermal sputtering, which are available commercially, those with smaller gold film thickness, d_{gold}, have smaller roughness values (Garnaes et al., 1990; Chiarello et al., 1992). Because the apparent distribution half-width, σ, of the marker atoms in films deposited on such mirrors decreases with σ_r, mirrors with smaller d_{gold} should be used whenever possible. However, we certainly cannot go to the limit of $d_{gold} = 0$. The question then arises, how small a value of d_{gold} is too small? To answer this question, reflectivity profiles were calculated and compared for different values of d_{gold}. The objective was to find the smallest value of d_{gold} that can still support reflectivity, at least in the angular range $\theta < \theta_c$. Fig. 6 shows the result of these calculations for d_{gold} in the 100–1000 Å range, with the roughness parameter, σ_r, set to zero. The calculations show that for $\theta < \theta_c$, the 200-Å-thick mirror has a reflectivity profile that is superimposable on that for the 1000-Å mirror. However, when mirror thickness is reduced to 100 Å, reflectivity falls significantly at $\theta < \theta_c$ and is larger at $\theta > \theta_c$ than that observed for the thicker mirrors. Based on calculated reflectivity profiles where d_{gold} was changed systematically (Fig. 6), we suggest that mirrors with a gold layer thickness between 200 Å and 300 Å are

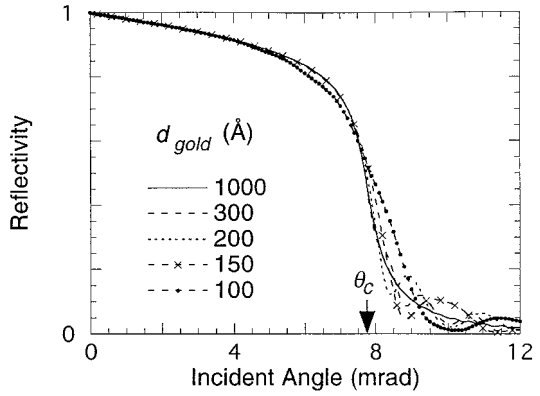

FIGURE 6 The effect of gold mirror thickness, d_{gold}, on reflectivity from a flat, three-layer system consisting of air, gold, and bulk silicon and calculated by using Eqs. 11 and 12. θ_c is the critical angle of the gold layer. Refractive indices for gold and silicon are reported in the legend to Fig. 3.

optimal for use in variable-period XSW measurements. Thinner mirrors do not reflect x-rays efficiently, whereas the thicker mirror is likely to be too rough.

Fluorescence yield profile for systems with rough interfaces

In previous variable-period XSW studies, Eq. 20, developed for systems with flat interfaces, was used to calculate the marker atom layer fluorescence yield profile (Bedzyk et al., 1989; Wang et al., 1991, 1994a, b). The implicit assumption in such cases was that all interfaces in the system are flat. Let us now calculate the fluorescence yield profile, $\Upsilon(\theta)$, for a multilayer system with rough interfaces. The local or intrinsic distribution function of the marker atom layer is $\rho_{in}(z_{in}) = \rho_{in}(z - z')$, and the interfacial roughness profile is described by $P(z')$ in Eq. 21. The corresponding fluorescence yield profile is calculated as

$$\Upsilon(\theta) = \int I_m(\theta, z)\left[\int \rho_{in}(z - z')P(z')\mathrm{d}z'\right]\mathrm{d}z \equiv \int I_m(\theta, z)\rho(z)\mathrm{d}z, \tag{31}$$

where $\rho(z)$ [$= \int \rho_{in}(z - z')P(z')\mathrm{d}z'$] is the convolution of the intrinsic distribution function and the interfacial roughness profile. As shown in Eq. 30, the variance of the $\rho(z)$ distribution, σ^2, is the sum of the variance of the $\rho_{in}(z_{in})$ distribution, σ_{in}^2, and of the $P(z')$ distribution, σ_r^2.

NUMERICAL MODELING

In the following section, calculations performed to simulate real samples examined by the XSW technique are presented, using parameter values similar to those obtained in actual experiments. Thus the sample used in these calculations consists of a lipid adlayer on a gold mirror in air. The gold mirror is deposited on bulk silicon, and a d_{gold} value of 280 Å was used because, as illustrated, this represents the best compromise as far as roughness and reflectivity are concerned. The refractive indices used for gold, lipid, and silicon are those presented in the legend to Fig. 3, and the interfacial roughness effect on x-ray reflectivity is accounted for by means of the Nevot-Croce factor, r_{NC}.

Truncated marker atom distribution

To calculate the fluorescence yield profile of a multilayer system with interfacial roughness, Eq. 31 is used, incorporating a Gaussian (Bedzyk et al., 1989; Wang et al., 1994a, b; Kirchner et al., 1995), to describe the laterally averaged distribution of marker atoms in the adlayer above the mirror surface as follows:

$$\rho(z) = \exp[-(z - \mu_g)^2/2\sigma_g^2], \tag{32}$$

where μ_g is the position of maximum probability in the distribution and σ_g is the Gaussian standard deviation. As noted, σ, which is what is measured experimentally, convolutes intrinsic width, σ_{in}, with the roughness of the mirror surface, σ_r (Eq. 30). Furthermore, for Gaussians that are truncated by natural boundaries at $z = 0$ and $z = d_L$, the distribution of the marker atoms is more effectively described by the first moment, $\langle z\rangle$, and the second moment, $\sigma = \langle z^2\rangle - \langle z\rangle^2$, calculated as

$$\langle z\rangle = \frac{\int_0^{d_L} z\rho(z)\mathrm{d}z}{\int_0^{d_L}\rho(z)\mathrm{d}z} = \mu_g + \sigma_g^2/C[\exp(-\mu_g^2/2\sigma_g^2) - \exp(-(d_L - \mu_g)^2/2\sigma_g^2)] \tag{33}$$

and

$$\langle z^2\rangle - \langle z\rangle^2 = \frac{\int_0^{d_L}(z^2 - \langle z\rangle^2)\rho(z)\mathrm{d}z}{\int_0^{d_L}\rho(z)\mathrm{d}z} = \sigma_g^2\{1 - [\mu_g\exp(-\mu_g^2/2\sigma_g^2) + (d_L - \mu_g)\exp(-(d_L - \mu_g)^2/2\sigma_g^2)]/C\} - (\langle z\rangle - \mu_g)^2, \tag{34}$$

where $C = \sigma_g(\pi/2)^{1/2}[\mathrm{erf}(\mu_g/2^{1/2}\sigma_g) + \mathrm{erf}((d_L - \mu_g)/2^{1/2}\sigma_g)]$ is the normalization factor and $\mathrm{erf}(x)$ [$= (2/\pi^{1/2})\int_0^x exp(-t^2)\mathrm{d}t$] is the error function. For a sharp Gaussian distribution function centered far from the adlayer boundaries, where $\mu_g/\sigma_g \gg 1$ and $(d_L - \mu_g)/\sigma_g \gg 1$, and where truncation is irrelevant, Eqs. 33 and 34 reduce to the result for a simple, complete Gaussian where $\langle z\rangle = \mu_g$ and $\langle z^2\rangle - \langle z\rangle^2 = \sigma_g^2$.

To demonstrate the problem associated with using μ_g and σ_g to describe a truncated Gaussian distribution function, the fluorescence yield profiles, calculated using Eqs. 18–20 and 31, for two truncated Gaussian distribution functions are shown in Fig. 7. The corresponding Gaussian parame-

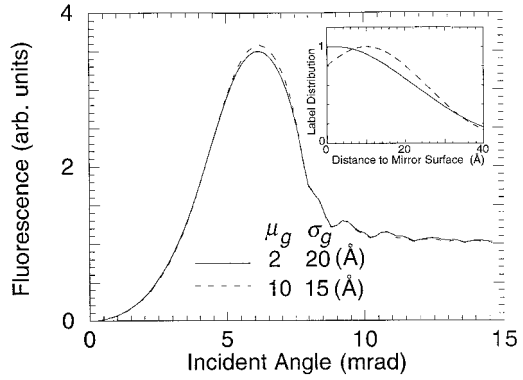

FIGURE 7 The effect of using truncated Gaussian distribution functions on calculated fluorescence yield profile. The profiles were generated based on typical x-ray standing-wave measurements using Eqs. 18–20 and 25, and the following conditions: gold mirror thickness, d_{gold} = 280 Å; organic adlayer thickness, d_L = 80 Å; interfacial roughness, σ_r = 5.6 Å. The Gaussian distribution functions in real space are illustrated in the inset. The corresponding $\langle z \rangle$ and σ values are 16.7 Å and 12.4 Å for distribution 1 (*solid line*, *inset*), and 16.4 Å and 10.9 Å for distribution 2 (*dashed line*, *inset*). Sample composition and refractive indices for gold, lipid adlayer, and silicon are as reported in the legend to Fig. 3. The critical angle of the gold mirror, θ_c, is 7.73 mrad.

ters are μ_g = 2 Å, σ_g = 20 Å (distribution 1, *solid line* in Fig. 7) and μ_g = 10 Å, σ_g = 15 Å (distribution 2, *dashed line* in Fig. 7). The two fluorescence yield profiles are quite similar, and indeed are indistinguishable experimentally, despite the fact that the μ_g and σ_g parameters for the two distributions are decidedly different. However, the calculated moments for the two truncated distributions are quite similar: $\langle z \rangle$ = 16.7 Å, σ = 12.4 Å for distribution 1, and $\langle z \rangle$ = 16.4 Å, σ = 10.9 Å for distribution 2. This comparison serves to highlight the problem of using μ_g and σ_g to describe distributions that are severely truncated. In such cases, it is misleading to report μ_g and σ_g. Rather, the first and second moments, calculated from μ_g and σ_g using Eqs. 33 and 34, respectively, are the appropriate descriptive parameters. Indeed, the fluorescence yield profile is sensitive to the first and second moments of the distribution, which, in the limit of a sharp distribution where $\mu_g/\sigma_g \gg 1$, reduce to μ_g and σ_g, respectively.

Numerical calculations

As stated in the Introduction, the physical quantities that are measured in a typical variable-period XSW experiment are angle-dependent x-ray reflectivity and fluorescence yield profiles. According to Eqs. 11 and 25, x-ray reflectivity depends strongly on the thickness of the organic adlayer, d_L, and interfacial roughness, σ_r. From Eqs. 18–19 and 25, the electric field intensity of the x-ray standing wave inside the organic adlayer also depends on d_L and σ_r. Accordingly, the x-ray fluorescence yield profile depends both on d_L and σ_r, as well as on the moments, $\langle z \rangle$ and $\langle z^2 \rangle - \langle z \rangle^2$, of the marker atom distribution function. In the following section, we show quantitatively how d_L, σ_r, $\langle z \rangle$, and σ affect x-ray reflectivity and fluorescence yield profiles by numerical calculations, to better understand the relation between these measured quantities and the physical properties of the sample. Reflectivity also depends on the thickness of the gold layer, d_{gold}, as was shown in Fig. 6. However, based on our calculations using typical experimental values of d_{gold} (calculations not shown), the fluorescence yield profile dependence on d_{gold} is insignificant compared to its dependence on d_L, σ_r, $\langle z \rangle$, and σ. In what follows, only the effects of the latter four parameters on reflectivity and fluorescence are examined.

The effect of organic adlayer thickness on reflectivity

Fig. 8 shows four theoretical reflectivity profiles calculated using Eqs. 9–12 and 25 for different adlayer thicknesses, d_L, with d_{gold} = 280 Å and σ_r = 5.6 Å. The reflectivity profiles for d_L values of 80 Å and 100 Å are similar, despite the fact that the thickness of the adlayers differs by 20 Å. In contrast, the profiles for d_L = 150 Å and 300 Å show that the larger thickness introduces noticeable oscillations at lower angles. The latter can be understood as follows. Consider the three-layer (air/lipid/gold) system in Fig. 2. X-rays with incident angles $\theta < \theta_c$ at the air/lipid interface are either reflected (rays labeled $A^{R,(0)}_{m-1,m}$ in Fig. 2) or transmitted into the adlayer. The latter are then reflected from the lipid/gold interface and then transmitted back into air at the lipid/air interface (rays labeled $A^{R,(1)}_{m-1,m}$ in Fig. 2). The reflectivity $R_{1,2}$ (in Eq. 12) can then be calculated from the sum of the electric fields of the directly reflected x-rays ($A^{R,(0)}_{m-1,m}$) and all of those x-rays passing through the adlayer and transmitted back into air ($A^{R,(n)}_{m-1,m}$, n = 1, 2, . . . , ∞): $R_{1,2} = |\Sigma_{n=0}^{\infty} A^{R,(n)}_{m-1,m}|^2$. Each time an x-ray wave travels down into and is reflected back out of the lipid adlayer, its phase changes by $2k_1 d_L(\theta^2 - \theta_{2c}^2)^{1/2}$ (shown in the exponential function in Eq. 11). The oscillations in the reflec-

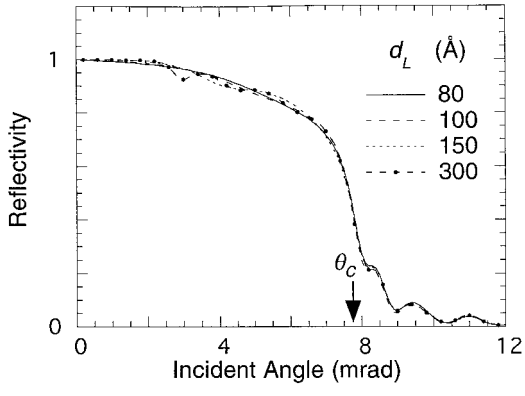

FIGURE 8 The effect of organic adlayer thickness, d_L, on calculated reflectivity profile. The profiles were generated based on typical x-ray reflectivity measurements, using Eqs. 9–12 and 25 and the following conditions: gold mirror thickness, d_{gold} = 280 Å; mirror roughness, σ_r = 5.6 Å. Sample composition and refractive indices used for gold, lipid adlayer, and silicon are as reported in the legend to Fig. 3. The critical angle of the gold mirror, θ_c, is indicated.

tivity curve arise from interference between the reflected x-rays ($A^{R,(n)}_{m-1,m}$, $n = 0, 1, 2, \ldots, \infty$), each having a different optical path and a different phase. To generate one full period of oscillation in the reflectivity profile within the angular range, $\Delta\theta$, for an adlayer of thickness d_L, the corresponding change in phase must be 2π. Specifically,

$$\Delta(2k_1 d_L(\theta^2 - \theta_{2c}^2)^{1/2}) \approx \frac{2k_1 d_L \theta \Delta\theta}{(\theta^2 - \theta_{2c}^2)^{1/2}} = 2\pi. \quad (35)$$

Therefore,

$$d_L = \frac{\pi(\theta^2 - \theta_{2c}^2)^{1/2}}{k_1 \theta \Delta\theta} = \frac{\lambda(\theta^2 - \theta_{2c}^2)^{1/2}}{2\theta\Delta\theta}, \quad (36)$$

where $k_1 = 2\pi/\lambda$. Solving Eq. 36 for $\Delta\theta = \theta_c - \theta_{2c} \approx 5.5$ mrad, $\theta \approx 5$ mrad, and $\lambda = 1.265$ Å (9.8 keV), we find that $d_L \approx 100$ Å. Thus, to observe one or more periods of oscillation in the reflectivity profile for 1.265-Å x-rays, the thickness of the organic adlayer must be equal to or greater than 100 Å, as seen in Fig. 8. (We note that the amplitude of the oscillations increases as d_L increases, because of a stronger interference effect. Conversely, from Fig. 8, the effect of d_L on the reflectivity curve is rather small when d_L is less than 100 Å. These calculations highlight the fact that the uncertainty associated with d_L values obtained by fitting to reflectivity profile data is quite large for films with $d_L \leq$ 100 Å. In fact, recent studies on small proteins (carbonic anhydrase and cytochrome *c*) deposited directly on x-ray mirror surfaces, forming a monolayer of thickness ~30 Å, show that the uncertainty in d_L values extracted from reflectivity profile can be as large as 30 Å.)

The effect of interfacial roughness on reflectivity

The manner in which interfacial roughness affects reflectivity is shown in Fig. 9 as a series of profiles calculated from Eqs. 9–12 and 25 and different values of interfacial roughness σ_r. In each case, d_{gold} is 280 Å and d_L is 80 Å. Clearly, interfacial roughness reduces the magnitude of the calculated reflectivity over much of the angular range studied. Physically, interfacial roughness gives rise to diffuse scattering and reduces specular reflectivity (measured in the x-ray incident plane).

It is evident that interfacial roughness has the effect of shifting the reflectivity curves to lower angles (Fig. 9). Consequently, the angle at which the reflectivity curve falls off most rapidly, and thus the critical angle for an ideally flat interface, decreases as roughness increases. This suggests that the apparent critical angle for a rough interface is smaller than that for a perfectly flat interface.

The effect of organic adlayer thickness on fluorescence yield profile

To show how adlayer thickness impacts on fluorescence, $\Upsilon(\theta)$ profiles have been calculated using Eqs. 18–20 and 25 for three different d_L values (Fig. 10). In each case, σ_r is 5.6 Å, $\langle z \rangle$ is 50 Å, and σ is 7 Å. The results show that for identical marker atom distributions, different adlayer thicknesses give rise to very different fluorescence yield profiles. This d_L modulation effect establishes the basis for requiring d_L as a fitting parameter in the analysis of fluorescence data. Accordingly, it is an important tool in the determination of d_L, especially for thin adlayers, where reflectivity is completely insensitive to and of little use in the determination of film thickness (Fig. 8). Quantitatively, we find the uncertainty in d_L determined from fluorescence profile fitting ranges from 1 to 5 Å for d_L values of ~80 Å with a relative counting error of 0.5% (Itri et al., 1997). This highlights the utility of fluorescence yield profile data in providing reliable estimates of d_L.

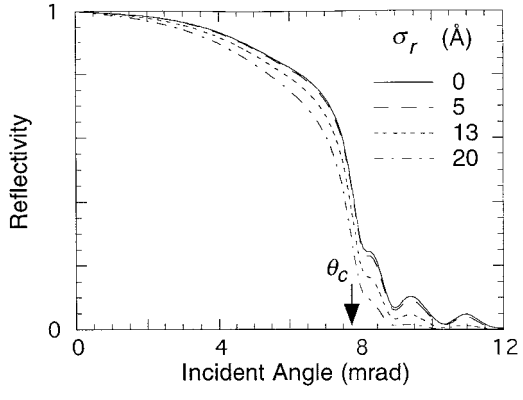

FIGURE 9 The effect of mirror roughness, σ_r, on calculated reflectivity profile. The profiles were generated based on typical x-ray reflectivity measurements, using Eqs. 9–12 and 25 and the following conditions: gold mirror thickness, d_{gold} = 280 Å; organic adlayer thickness, d_L = 80 Å. Sample composition and refractive indices used for gold, lipid adlayer, and silicon are as reported in the legend to Fig. 3. The critical angle of the gold mirror, θ_c, is indicated.

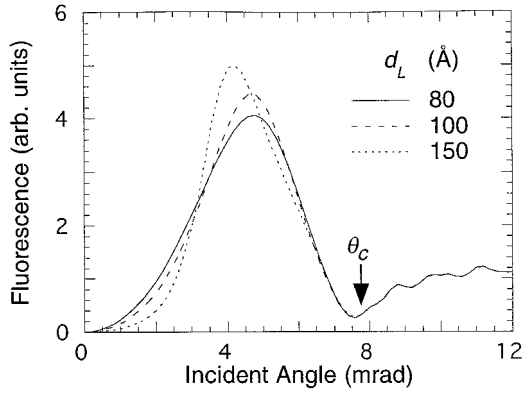

FIGURE 10 The effect of organic adlayer thickness, d_L, on calculated fluorescent yield profile. The profiles were generated based on typical x-ray standing wave measurements, using Eqs. 18–20 and 25 and the following conditions: gold mirror thickness, d_{gold} = 280 Å; mirror roughness, σ_r = 5.6 Å; marker atom position, $\langle z \rangle$ = 50 Å; distribution half-width, σ = 7 Å. Sample composition and refractive indices used for gold, lipid adlayer, and silicon are as reported in the legend to Fig. 3. The critical angle of the gold mirror, θ_c, is indicated.

It was surprising to us at first to find that the fluorescence yield profile had such a strong dependence on d_L. However, this can be explained by inspecting the formulas describing the fluorescence yield profile. According to Eqs. 18 and 19, the intensity of the x-ray standing-wave field inside the adlayer is proportional to the intensity of the electric field just below the air/adlayer interface, $|E_2(d_2)|^2$. From Eq. 15, the effective transmission coefficient at the air/adlayer interface is $t_{1,2} = E_2(d_2)/E_0 = (1 - F^R_{1,2}r_{1,2})/F^T_{1,2}$, where $F^R_{1,2}$ and $F^T_{1,2}$ are the Fresnel reflection and transmission coefficients, respectively, and $r_{1,2} = [F^R_{1,2} + r_{2,3}\exp(-2ik_1\theta_2 d_2)]/[1 + F^R_{1,2}r_{2,3}\exp(-2ik_1\theta_2 d_2)]$ (note $d_2 \equiv d_L$) from Eq. 11. Therefore, different values of d_L yield different phase factors, $2k_1\theta_2 d_2$, in $r_{1,2}$ that eventually give rise to different electric field intensities, $|E_2(d_2)|^2$, and fluorescence yield profiles. An interesting consequence of this occurs when d_L and the x-ray wavelength are such that the denominator in $r_{1,2}$ is very small (the resonance condition), and a resonance-enhanced x-ray standing-wave field is formed (Wang et al., 1992) for which the XSW electric field intensity, $|E_2(d_2)|^2$, at a certain angle can be an order of magnitude or more larger than that at the same angle for a sample with no adlayer present.

The effect of interfacial roughness on fluorescence yield profile

To examine how interfacial roughness affects the fluorescence yield profile, the results of calculations using Eqs. 18–20 and 25 for three different values of σ_r are shown in Fig. 11 for $d_L = 80$ Å, $\langle z\rangle = 50$ Å, and $\sigma = 7$ Å. It is evident that a larger interfacial roughness results in a smaller fluorescence signal in the 2–8-mrad range. The specular x-ray reflectivity at the adlayer/gold interface is reduced by interfacial roughness. Because x-ray standing waves are formed by the interference of the incident and specularly reflected x-rays, the standing-wave electric field intensity (Eqs. 18 and 19) and corresponding fluorescence yield (Eq. 20) are decreased as a result of roughness. One interesting feature of the σ_r effect on fluorescence is that it attenuates the fluorescence yield more on the high-angle side of the fluorescence peak position θ_{max}. This is because the reduction in reflectivity brought on by interfacial roughness lessens at smaller angles, and is largest in the vicinity of θ_c (Fig. 9). However, for $\theta > \theta_c$, where reflectivity is low, the total electric field intensity exciting fluorescence is dominated by the incident x-ray intensity (Eqs. 18 and 19). Hence the fluorescence yield depends little on interfacial roughness in this angular range.

The effect of marker atom position on fluorescence yield profile

To show how the average position of the marker atom layer in the adlayer affects the fluorescence yield profile, calculations are shown in Fig. 12 using Eqs. 18–20 and 25 for three marker positions, $\langle z\rangle$, with $d_{gold} = 280$ Å, $\sigma_r = 5.6$ Å, $d_L = 100$ Å, and $\sigma = 7$ Å. Thus, shifting the marker layer further away from the mirror surface by increasing $\langle z\rangle$ causes a drop in the angle where the fluorescence yield profile reaches a maximum θ_{max}. This effect can be understood in the following way. Both reflectivity, $R_{2,3}(\theta)$, and phase shift, $\phi^R_2(\theta)$, in Eq. 18 change rather slowly with θ, for $\theta < \theta_c$. However, the phase factor $2k_1 z(\theta^2 - \theta^2_{2c})^{1/2}$ depends strongly on θ. Substituting Eq. 18 into Eq. 20 and assuming, for simplicity, that the distribution is relatively sharp, such that $\rho(z) \approx \delta(z - \langle z\rangle)$ corresponding to a delta function, the fluorescence yield profile remains basically unchanged for a small change in θ, $\Delta\theta$, as long as the product $2k_1\langle z\rangle(\theta^2 -$

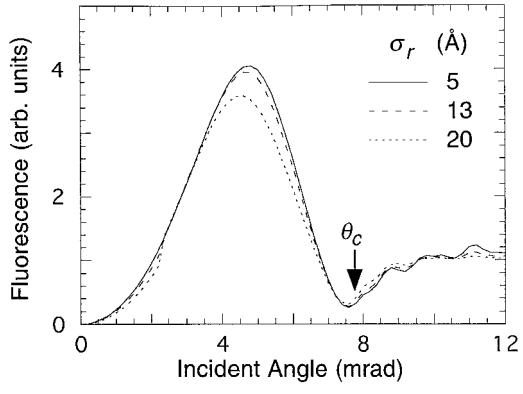

FIGURE 11 The effect of mirror roughness, σ_r, on calculated fluorescent yield profile. The profiles were generated based on typical x-ray standing-wave measurements, using Eqs. 18–20 and 25 and the following conditions: gold mirror thickness, $d_{gold} = 280$ Å; organic adlayer thickness, $d_L = 80$ Å; marker atom position, $\langle z\rangle = 50$ Å; distribution half-width, $\sigma = 7$ Å. Sample composition and refractive indices used for gold, lipid adlayer, and silicon are as reported in the legend to Fig. 3. The critical angle of the gold mirror, θ_c, is indicated.

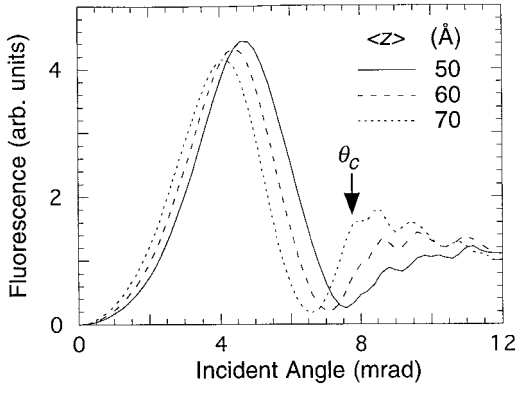

FIGURE 12 The effect of marker atom position, $\langle z\rangle$, in the lipid adlayer above the reflecting mirror surface on calculated fluorescent yield profile. The profiles were generated based on typical x-ray standing-wave measurements, using Eqs. 18–20 and 25 and the following conditions: gold mirror thickness, $d_{gold} = 280$ Å; organic adlayer thickness, $d_L = 100$ Å; mirror roughness, $\sigma_r = 5.6$ Å; distribution half-width, $\sigma = 7$ Å. Sample composition and refractive indices used for gold, lipid adlayer, and silicon are as reported in the legend to Fig. 3. The critical angle of the gold mirror, θ_c, is indicated.

$\theta_{2c}^2)^{1/2}$ remains constant. This is equivalent to requiring that a small change in $\langle z\rangle$, $\Delta\langle z\rangle$, satisfies the following condition:

$$\frac{\Delta\langle z\rangle}{\langle z\rangle} = \frac{-\theta\Delta\theta}{\theta^2 - \theta_{2c}^2}. \quad (37)$$

By way of example, let us calculate $\Delta\langle z\rangle$ for a typical sample where $\theta_{2c} \approx 2.24$ mrad, $\theta = \theta_{max} \approx 4$ mrad, and $\langle z\rangle \approx 50$ Å. Accordingly, when $\Delta\theta = \Delta\theta_{max} = -0.1$ mrad, we find that $\Delta\langle z\rangle = 1.8$ Å. Therefore, an uncertainty of 0.1 mrad in the measurement of incident angle translates into an uncertainty of ~2 Å in the marker atom position. Equation 37 is also applicable to fluorescence data for thick films, which have multiple peaks in the fluorescence yield profiles (Wang et al., 1991, 1994a). The sensitivity of the fluorescence yield profile to $\langle z\rangle$ in the thick adlayers was examined numerically (Wang et al., 1991), and the results are in good agreement with those reported here.

The effect of marker atom distribution width on fluorescence yield profile

How the distribution half-width, σ, of marker atoms affects fluorescence yield profiles was examined by performing calculations using Eqs. 18–20 and 25 with three values of σ, setting $\sigma_r = 5.6$ Å, $d_L = 100$ Å, and $\langle z\rangle = 50$ Å (Fig. 13). Also included is a calculation using $\sigma = 30$ Å, $\sigma_r = 0$ Å, $d_L = 100$ Å, and $\langle z\rangle = 50$ Å, to remove the roughness effect and examine more directly the effect of distribution width. The results show that a finite σ dampens oscillation and broadens the peak in the fluorescence yield profile. A perusal of Eq. 20 shows that when the distribution function, $\rho(z)$, is a δ-function, the fluorescence yield $Y(\theta)$ (represented in Fig. 13 as a *solid line*) is proportional to the electric field intensity, $I_2(\theta, z)$. In contrast, for a sample containing marker atoms with a nonzero distribution width, $Y(\theta)$ is the average of $I_2(\theta, z)$ measured in the z direction across the entire adlayer, weighted by the corresponding distribution function $\rho(z)$. Naturally, this averaging procedure smoothes out oscillations in the fluorescence profile, and when the distribution is sufficiently broad, it eliminates the dip in the curve near θ_c. Consequently, the corresponding fluorescence peaks are broadened.

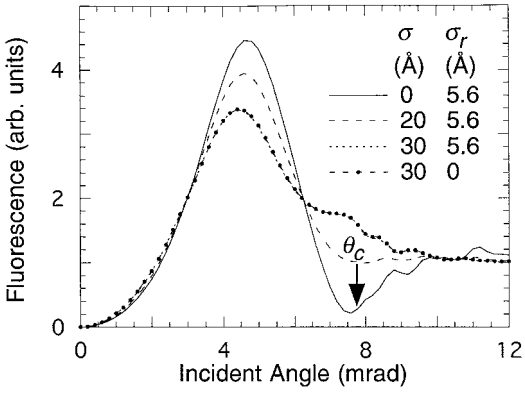

FIGURE 13 The effect of marker atom distribution width, σ, and of mirror roughness, σ_r, on calculated fluorescence yield profile. The profiles were generated based on typical x-ray standing-wave measurements, using Eqs. 18–20 and 25 and the following conditions: gold mirror thickness, $d_{gold} = 280$ Å; organic adlayer thickness, $d_L = 100$ Å; marker atom position, $\langle z\rangle = 50$ Å. Sample composition and refractive indices used for gold, lipid adlayer, and silicon are as reported in the legend to Fig. 3. The critical angle of the gold mirror, θ_c, is indicated.

It is important to compare the effects on the fluorescence yield profile of the two parameters that are related to the disorder in the sample: σ_r, the roughness of the mirror surface, and σ_{in}, the uncertainty in the position of the marker atoms. When marker atom distribution is nearly uniform within the adlayer, the corresponding fluorescence yield profile is still reasonably well defined. This is illustrated by the dotted line in Fig. 13, which was calculated with a broad distribution width, $\sigma = 30$ Å, and a roughness value, $\sigma_r = 5.6$ Å. To demonstrate clearly the sole effect of σ on the fluorescence yield profile, we also plot the profile calculated with $\sigma = 30$ Å and $\sigma_r = 0$ Å (*solid circles* in Fig. 13). These results show that when $\sigma \gg \sigma_r$, the latter σ_r has a negligible effect on the fluorescence yield profile. It should be stressed, however, that when the roughness of the interface is too large ($\sigma_r \gg 1/q_z$), the theory describing the roughness fails (de Boer, 1991). This arises because of random reflection from a very rough interface where the phase shift, $\Phi_2^R(\theta)$, in Eq. 18 becomes random. Hence the incident and reflected x-rays are no longer coherently related, the XSW electric field is poorly established, and the fluorescence profile is severely broadened.

CONCLUSIONS

We have examined the effects of interfacial roughness on x-ray reflectivity and fluorescence, and of layer boundary truncation on distribution functions used in data analysis of the variable-period XSW method. The effects have been evaluated from the point of view of basic theory and numerical modeling. The purpose has been to gain a better understanding of the method with a view to more effectively using it to elucidate membrane structure.

In terms of interfacial roughness, we have shown that the Nevot-Croce factor gives a better fit to our x-ray reflectivity data than the customarily used Debye-Waller factor. Furthermore, it was shown that interfacial roughness, σ_r, is convoluted with the intrinsic marker atom distribution width, σ_{in}, into the apparent distribution width, σ, in the following way: $\sigma^2 = \sigma_{in}^2 + \sigma_r^2$, where σ is obtained from the fluorescence data. Because σ_r is obtained from reflectivity data, it is possible to deconvolute the latter relationship and to obtain a measure of σ_{in}, the quantity of interest in most XSW studies of model membranes. Our calculations and experience suggest that mirrors with a gold layer thickness between 200 Å and 300 Å should be used in future XSW experiments. This thickness range is consistent with high reflecting power and a minimum surface roughness, which, in turn, is associated with the smallest σ_{in}. With regard to

marker atom distribution, we have shown that the measured fluorescence yield profile is sensitive to the mean position or first moment and variance or second moment of the corresponding distribution. Accordingly, the distribution characteristics are better described by these parameters. Because of problems associated with truncated distributions, the commonly used Gaussian parameters, μ_g and σ_g, can be misleading and are not recommended.

Our numerical simulations show that interfacial roughness decreases reflectivity over the entire θ range of interest in XSW measurements. The effects of adlayer thickness, d_L, interfacial roughness, σ_r, and marker atom position, $\langle z \rangle$, and distribution half-width, σ, on fluorescence yield profile were also studied. These show that elevating $\langle z \rangle$ causes a shift in the fluorescence peak to lower angles. In contrast, increasing the distribution half-width, σ, and increasing interfacial roughness, σ_r, have the same result of lowering the fluorescence yield curve, with the effect most pronounced below the critical angle of gold. Furthermore, whereas σ tends to broaden the entire fluorescence peak, σ_r has its attenuating effect more on the high angle side of fluorescence peak. Finally, modulation of the XSW electric field intensity and the corresponding fluorescence yield profile by adlayer thickness, d_L, is quite strong. This facilitates the use of d_L as a fitting parameter in fluorescence data analysis, which is more sensitive to d_L than to reflectivity, particularly for adlayer films less than 100 Å thick.

Dr. S. Kirchner's participation in the early stages of this project is acknowledged. The authors thank Dr. Jin Wang for helpful discussions.

This work was supported by grants from the National Institutes of Health (DK36849 and DK46295) and the Petroleum Research Foundation of the American Chemical Society (30537-AC7) to MC. RI and RZ, respectively, thank the Fundaçao de Amparo a Pesquisa do Estado de São Paulo (FAPESP/SP) and the Graduate School of The Ohio State University for postdoctoral fellowships.

REFERENCES

Bedzyk, M. J., D. H. Bilderback, G. M. Bommarito, M. Caffrey, and J. S. Schildkraut. 1988. X-ray standing waves: a molecular yardstick for biological membranes. *Science.* 241:1788–1791.

Bedzyk, M. J., G. M. Bommarito, M. Caffrey, and T. L. Penner. 1990. Diffuse-double layer at a membrane-aqueous interface measured with x-ray standing waves. *Science.* 248:52–56.

Bedzyk, M. J., G. M. Bommarito, and J. S. Shildkraut. 1989. X-ray standing waves at a reflecting mirror surface. *Phys. Rev. Lett.* 62: 1376–1379.

Chiarello, R. P., H. K. Kim, T. Roberts, D. J. Miller, R. T. Kampwirth, K. E. Gray, and H. You. 1992. In-situ x-ray reflectivity study on growth dynamics of sputter deposited gold on silicon. *Mater. Res. Soc. Symp. Proc.* 237:411–415.

Cowley, R. A., and T. W. Ryan. 1987. X-ray scattering studies of thin films and surfaces: thermal oxides on silicon. *J. Phys. D Appl. Phys.* 20: 61–68.

de Boer, D. K. G. 1991. Glancing-incidence x-ray fluorescence of layered materials. *Phys. Rev. B.* 44:498–511.

de Boer, D. K. G. 1994. Influence of the roughness profile on the specular reflectivity of x-rays and neutrons. *Phys. Rev. B.* 49:5817–5820.

de Boer, D. K. G. 1995. X-ray reflection and transmission by rough surfaces. *Phys. Rev. B.* 51:5297–5305.

de Boer, D. K. G. 1996. X-ray scattering and x-ray fluorescence from materials with rough surfaces. *Phys. Rev. B.* 53:6048–6064.

Dietrich, S., and A. Haase. 1995. Scattering of x-rays and neutrons at interfaces. *Phys. Rep.* 260:1–138.

Garnaes, J., F. E. Christensen, F. Besenbacher, E. Laegsgaard, and I. Stensgaard. 1990. Scanning tunneling microscopy studies of thin foil x-ray mirrors. *Opt. Eng.* 29:666–671.

Itri, R., R. Zhang, and M. Caffrey. 1997. Spatial resolution of the variable-period x-ray standing wave method as applied to model membranes. *Biophys. J.* 73:1506–1515.

Kirchner, S., J. Wang, Z. Yin, and M. Caffrey. 1995. X-ray standing waves as probes of surface structure: incident beam energy effects. *J. Appl. Phys.* 78:2311–2322.

Krol, A., C. J. Sher, and Y. H. Kao. 1988. X-ray fluorescence of layered synthetic materials with interfacial roughness. *Phys. Rev. B.* 38: 8579–8591.

Nevot, L., and P. Croce. 1980. Surface characterization by grazing x-ray reflection. Application to the study on some silicate glass polishing. *Rev. Phys. Appl.* 15:761–779.

Parrat, L. G. 1954. Surface studies of solids by total reflection of x-rays. *Phys. Rev.* 95:359–369.

Penfold, J., and R. K. Thomas. 1990. The application of the specular reflection of neutrons to the study of surfaces and interfaces. *J. Phys. Condens. Matter.* 2:1369–1412.

Sinha, S. K., E. B. Sirota, S. Garoff, and H. B. Stanley. 1988. X-ray and neutron scattering from rough surfaces. *Phys. Rev. B.* 38:2297–2311.

Vidal, B., and P. Vincent. 1984. Metallic multilayers for x-rays using classical thin-film theory. *Appl. Opt.* 23:1794–1801.

Wang, J. 1994. X-ray standing waves and their use in characterizing biologically relevant thin film systems. Doctoral dissertation. The Ohio State University, Columbus, OH.

Wang, J., M. J. Bedzyk, and M. Caffrey. 1992. Resonance-enhanced x-rays in thin films: a structure probe for membranes and surface layers. *Science.* 258:775–778.

Wang, J., M. J. Bedzyk, T. L. Penner, and M. Caffrey. 1991. Structural studies of membranes and surface layers up to 1000 Å thick using x-ray standing waves. *Nature.* 354:377–380.

Wang, J., and M. Caffrey. 1995. Locating calcium in membranes with x-ray standing waves. *J. Am. Chem. Soc.* 117:3304–3305.

Wang, J., M. Caffrey, M. J. Bedzyk, and T. L. Penner. 1994a. Structure changes in model membranes monitored by variable-period x-ray standing waves: effect of Langmuir-Blodgett film thickness on thermal behavior. *J. Phys. Chem.* 98:10957–10968.

Wang, J., C. J. A. Wallace, I. Clark-Lewis, and M. Caffrey. 1994b. Structure characterization of membrane bound and surface adsorbed protein. *J. Mol. Biol.* 237:1–4.